Journal of Applied Physics

Cation distribution in $CuFe_2O_4$ nanoparticles: Effects of Ni doping on magnetic properties

Cite as: J. Appl. Phys. **120**, 142115 (2016); https://doi.org/10.1063/1.4961722
Submitted: 04 April 2016 . Accepted: 07 August 2016 . Published Online: 31 August 2016

Nguyen Kim Thanh, To Thanh Loan, Luong Ngoc Anh, Nguyen Phuc Duong, Siriwat Soontaranon, Nirawat Thammajak, and Than Duc Hien

AIP Publishing

Cation distribution in $CuFe_2O_4$ nanoparticles: Effects of Ni doping on magnetic properties

Nguyen Kim Thanh,[1] To Thanh Loan,[1,a)] Luong Ngoc Anh,[1] Nguyen Phuc Duong,[1] Siriwat Soontaranon,[2] Nirawat Thammajak,[2] and Than Duc Hien[1]
[1]*International Training Institute for Materials Science (ITIMS), Hanoi University of Science and Technology, Hanoi 100000, Vietnam*
[2]*Synchrotron Light Research Institute, 111 University Avenue, Suranaree, Muang, Nakhon Ratchasima 30000, Thailand*

(Received 4 April 2016; accepted 7 August 2016; published online 31 August 2016)

The $Cu_{1-x}Ni_xFe_2O_4$ nanoparticles (with $x = 0$, 0.3, 0.5, 0.7, and 1) were synthesized by using spray co-precipitation method at annealing temperature $T_a = 900\,^{\circ}C$ in air for 5 h. The crystal structure, microstructure, oxidation state, and magnetic properties of the samples were characterized by using X-ray diffraction, synchrotron X-ray diffraction, scanning electron microscopy, X-ray absorption spectroscopy, and vibrating sample magnetometer. It was shown that all the samples have cubic structure. Lattice constant and grain size decrease, while the Curie temperature T_C increases with increasing of Ni^{2+} content. A small amount of Fe^{2+} was found in all the samples. Cation distribution was determined by using a combination of magnetization measurements, extended X-ray absorption fine structure analysis, and Rietveld refinement from synchrotron X-ray diffraction data. It was indicated that Ni^{2+} ions occupy in octahedral site only, while Cu^{2+} ions distribute in both tetrahedral and octahedral sites. The variation of magnetic parameters is discussed based on Ni^{2+} concentration, grain size, the cation distribution, surface effect, and the presence of Fe^{2+} ion in the samples. *Published by AIP Publishing.* [http://dx.doi.org/10.1063/1.4961722]

I. INTRODUCTION

Ferrites are materials of important applications in the manufacture of electronic devices. Some interesting applications of these materials are in permanent magnets, magnetic media used in computers, recording devices, magnetic cards, electronic and microwave devices, high frequencies device and recently in biomedicine, and catalyst for environment.[1–3] The most important characteristic of ferrites is that their properties as well as structure are strongly affected by the compositional variability and synthesis method such as processing conditions and annealing temperature.[4,5] Hence, depending on the requirements of the ultimate application, various combinations of different properties can be obtained by blending a judicious choice of the simple ferrites in an appropriate ratio.

Copper ferrite is one of the most important ferrites with interesting physical properties and potential applications such as information storage, gas sensors, and catalyst production for clean energy and environmental treatment.[6–8] $CuFe_2O_4$ exists in two symmetry modifications (tetragonal and cubic) and has a mixed spinel structure with different cation distributions $(Cu_yFe_{1-y})_A[Cu_{1-y}Fe_{1+y}]_BO_4$ depending on the preparation methods and heat-treatment conditions.[9] For bulk samples prepared by a conventional ceramic method, on slow cooling from 900 °C to room temperature, y is as small as 0.03 and the crystal structure has a tetragonal symmetry due to Jahn–Teller distortion, but by quenching rapidly from 900 °C to room temperature $y \approx 0.2$, the crystal structure becomes a cubic symmetry.[10] This cation distribution greatly influences on the properties of copper ferrite, especially its magnetic properties. There are numerous methods for fabricating copper ferrite nanoparticles such as milling method, co-precipitation method, and hydrothermal method.[11–13] In our previous work,[14] cation distribution and magnetic properties of copper ferrite prepared by using a spray co-precipitation method with different annealing temperatures were investigated. The result indicated that with increasing annealing temperature (T_a), the distribution of Cu^{2+} in the tetrahedral (A) site (y) increases, reaches the maximum value at $T_a = 900\,^{\circ}C$, and leads to the increase in saturation magnetization. In this work, we focus on studying the influence of doping effect on cation distribution and magnetic properties of $CuFe_2O_4$ nanoparticles. The substitution of Cu^{2+} by Ni^{2+} was chosen because in the spinel structure, magnetic nickel ions tend to occupy the octahedral [B] site,[4] and therefore, it is convenient to study the distribution of copper ions between (A) and [B] sites. Moreover, nickel ferrite is widely used in magnetic technologies because of their large permeability at high frequency, high electrical resistivity, low eddy current and dielectric losses, chemical stability, and cost effectiveness.[1] Therefore, Cu-Ni ferrites can be expected to have the advantages of both mother ferrites.

The reported studies on nickel-copper ferrite indicated that Ni^{2+} ions locate only in the octahedral site, while Cu^{2+} ions can occupy in both (A) and [B] sites, but the distribution degree seems to be strongly dependent on the preparation method as well as on the experimental conditions and Ni/Cu ratios.[15–18] It is known that the structural and magnetic

This paper is part of the Special Topic "Cutting Edge Physics in Functional Materials" published in J. Appl. Phys. **120**, 14 (2016).
a)Author to whom correspondence should be addressed. Electronic mail: totloan@itims.edu.vn.

properties of spinel ferrites are affected by magnetic interactions and cation distribution in the tetrahedral and octahedral sites.[19] Hence, by changing the Ni/Cu concentration ratio, the exchange interactions and cation distribution are varied, leading to the change in the magnetic properties.

This paper presents a systematic study of the nickel doping effect on the crystal structure, microstructure, oxidation state, magnetic properties, and cation distribution of the $Cu_{1-x}Ni_xFe_2O_4$ nanoparticles (with $x = 0$, 0.3, 0.5, 0.7, and 1) prepared by using a spray co-precipitation method at an annealing temperature $T_a = 900\,^{\circ}C$. Various experimental techniques have been employed to determine the morphology, the valence states of copper and iron ions, as well as the structural and magnetization characterizations. Especially, the cation distribution was determined from synchrotron X-ray diffraction (SXRD) data using Rietveld refinement with the help of the extended X-ray absorption fine structure (EXAFS) and magnetization analyses. The Néel model and cation distributions were taken into consideration to explain the magnetic properties of the samples.

II. EXPERIMENT

The spray co-precipitation method was employed to fabricate the $Cu_{1-x}Ni_xFe_2O_4$ nanoparticles ($x = 0$, 0.3, 0.5, 0.7, and 1). The solutions of $Cu(NO_3)_2$ 0.1 M, $Ni(NO_3)_2$ 0.1 M, and $Fe(NO_3)_3$ 0.2 M were prepared from salts $Cu(NO_3)_2{\cdot}4H_2O$, $Ni(NO_3)_2{\cdot}4H_2O$, and $Fe(NO_3)_3{\cdot}6H_2O$ mixed in molar ratios Cu:Ni:Fe = $(1 - x)$: x:2 ($x = 0$, 0.3, 0.5, 0.7, and 1). A 0.8 M NaOH solution was prepared. The chemicals and reagents are supplied by Sigma-Aldrich with purity of 3 N. The mixed metal salt solution and NaOH solutions were sprayed via high pressure nozzles into a vessel containing NaOH 10^{-4} M to keep pH of the environment equal to 10. A reddish-brown precipitate in the colloidal form was obtained from this reaction. Precipitates were washed by deionized water until pH reached 7–8. The precipitates were collected and heated at 60 °C for 24 h. The as-synthesized powders were sintered at a high temperature of 900 °C for 5 h and then immediately quenched into ice-melting water. Nanoparticles were extracted by a permanent magnet and dried at 60 °C for 5 h.

X-ray powder diffraction (XRD) measurements were performed by using X-ray diffractometer (Siemens D5000, CuK_α radiation, and $\lambda = 1.5406$ Å). Synchrotron X-ray powder diffraction (SXRD) experiments were carried out at beamline Small/Wide Angle X-ray Scattering (SAXS/WAXS) of the Synchrotron Light Research Institute (Thailand) ($\lambda = 1.54$ Å). The diffraction data were analyzed using the Rietveld method with the help of the FullProf program.[20] The diffraction peaks were modeled by pseudo-Voigt function which is a sum of Gaussian and Lorentzian functions.[21] A standard of silicon was used to determine instrument broadening. The refinement fitting quality was checked by goodness of fit (χ^2) and weighted profile R-factor (R_{wp}).[22]

Field Emission-Scanning Electron Microscopy (FE-SEM) (JEOL JSM-7600 F) was used to examine the grain size and morphology.

X-ray absorption spectroscopy (XAS) measurements were performed at BL8 of the Synchrotron Light Research Institute (Thailand).[23] X-ray absorption near-edge spectroscopy (XANES) and extended X-ray absorption fine structure (EXAFS) spectra of the samples were measured at the Fe and Cu K edge in the transmission mode at room temperature. A double crystal monochromator Ge (220) was used to scan the energy of the synchrotron X-ray beam. The XAS spectra were baseline subtracted and normalized using the software package ATHENA.[24]

Magnetization curves were measured using a vibrating sample magnetometer (VSM) (ADE Technology—DMS 5000) in the temperature range of 87–900 K and applied magnetic fields up to 10 kOe.

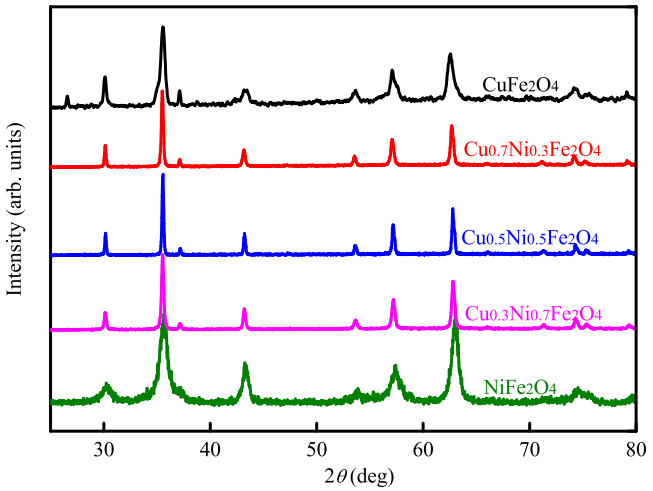

FIG. 1. X-ray diffraction patterns of the $Cu_{1-x}Ni_xFe_2O_4$ samples ($x = 0$, 0.3, 0.5, 0.7, and 1).

III. RESULTS AND DISCUSSION

A. Crystal structure, morphological analysis, and oxidation state

From XRD patterns (Fig. 1) and high-resolution SXRD patterns (Fig. 2), it is seen that the $Cu_{1-x}Ni_xFe_2O_4$ samples with $x = 0.3$, 0.5, 0.7, and 1 are phase pure without any signature of impurity. On the other hand, a small amount of

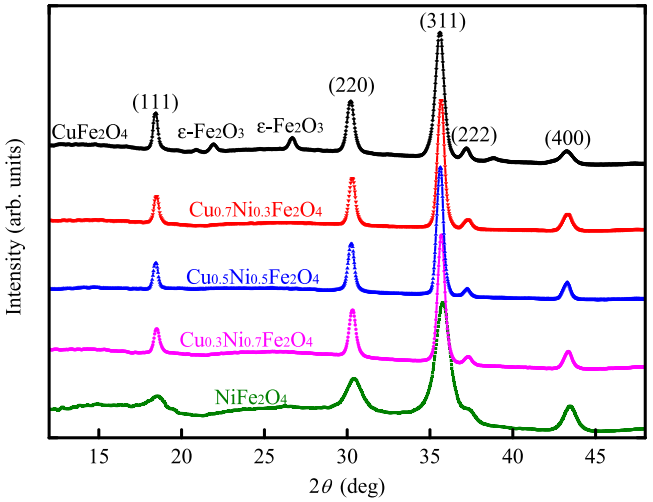

FIG. 2. Synchrotron X-ray diffraction patterns of the $Cu_{1-x}Ni_xFe_2O_4$ samples ($x = 0$, 0.3, 0.5, 0.7, and 1).

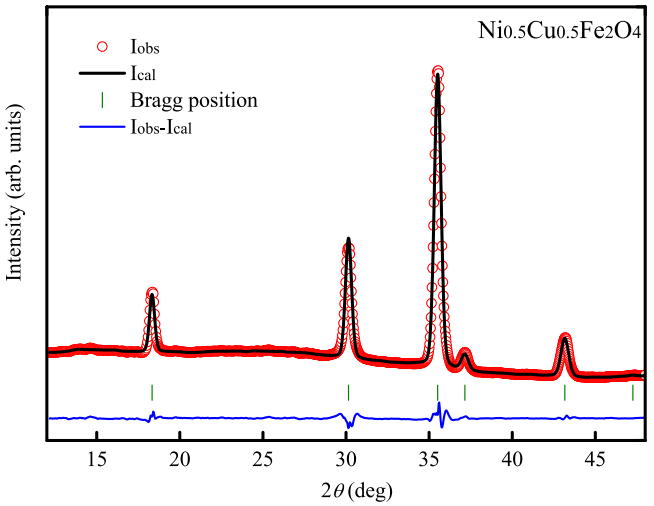

FIG. 3. Synchrotron diffraction pattern of $Cu_{0.5}Ni_{0.5}Fe_2O_4$ and processed by the Rietveld method. The experimental points as well as calculated and difference functions are indicated.

impurity was observed in the sample with $x = 0$. By using Rietveld refinement, this impurity is identified as ε-Fe_2O_3 with a concentration of ~5 mol. %. ε-Fe_2O_3 is rare Fe_2O_3 polymorph that may exist in nanosized samples obtained via soft chemical routes.[25]

All the samples are cubic and well refined in space group *Fd3m* with atoms in positions O in 32 *e*(*x, x, x*), A-site in 8*a*(1/8, 1/8, 1/8), and B-site in 16*d*(1/2, 1/2, 1/2). One of the SXRD patterns and its Rietveld refinement is shown in Fig. 3. The refined values of structural parameters, including lattice constant (*a*), unit-cell volume (*V*), and oxygen coordinate (*x*(O)), for the samples are given in Table I. The obtained values of oxygen coordinate are characteristic of a spinel-type structure.[26] The substitution of Ni^{2+} for Cu^{2+} leads to a decrease in lattice parameter as well as unit cell volume which can be explained by the difference in their ionic radii. The ionic radii of Ni^{2+} ion are smaller than that of Cu^{2+} ($r_{Cu}{}^{2+} = 0.71$ Å, $r_{Ni}{}^{2+} = 0.69$ Å for the tetrahedral site and $r_{Cu}{}^{2+} = 0.87$ Å, $r_{Ni}{}^{2+} = 0.83$ Å for the octahedral site).[27] This result is in a very good agreement with that reported previously.[18]

The microstructural parameters, including the average size of the coherent scattering region *D* (usually called the crystallite size) and lattice microstrains $\Delta a/a$ (where *a* is the lattice constant), were obtained by the analysis of the peak broadening. In our work, the average size of coherent scattering region and the microstrains was determined on applying the Rietveld method using the FullProf program with a condition that instrumental resolution function was provided. The obtained values of the microstructural parameters are listed in Table I. The lattice microstrain allows us to characterize the structure disorder of the samples. Substitution of Cu^{2+} by Ni^{2+} leads to the change of lattice microstrain. As seen in Table I, both the crystallite size and lattice microstrain first increase upon increasing of nickel substitution, reach a maximum value at $x = 0.5$, and then decrease with further increasing of *x*. The crystallite size distributes in nano-scale from 6 to 29 nm, in which the crystallite size of the $NiFe_2O_4$ sample is much smaller than that of the samples containing copper. This phenomenon can be explained due to the low melting temperature of the oxide compounds containing copper.[28] In these compounds, the copper ions with high mobility easily diffuse to form larger crystallites as well as grains.

The grain size and morphology of the $Cu_{1-x}Ni_xFe_2O_4$ samples characterized by SEM are shown in Fig. 4. It can be seen that the average grain size decreases with increasing Ni content. For the samples with $x = 0.7$ and 1, the majority of grains are nearly spherical with uniform shape, grain size distributes in ranges 20–30 nm and 5–15 nm, respectively, for $x = 0.7$ and 1, which are in good agreement with the average crystallite size *D* (given in Table I). It was also observed that the grains of these samples are agglomerated in the form of clusters due to high annealing temperatures and attractive forces such as those of magnetic dipole–dipole type, whereas for the samples with $x = 0$, 0.3, and 0.5, the crystals grew into polygonal blocks and the grain size distributes in ranges of 0.5–1 μm, 100–300 nm, and 100 nm, respectively. The grain sizes of these samples are much larger than the average crystallite sizes *D* calculated via Rietveld refinement (given in Table I); therefore, the grains may contain several crystallites.

Figure 5 shows the XANES spectra at Fe and Cu *K* edges of the $Cu_{1-x}Ni_xFe_2O_4$ samples and the oxide standards (ferrous oxide, hematite, cuprous oxide, and tenorite). The oxidation state of iron and copper in the samples was determined by comparing the absorption edge energy with those of the standards. As known, the higher oxidation state, the higher the chemical shift of the absorption edge. At the Cu *K* edge, the edge energy of the $Cu_{1-x}Ni_xFe_2O_4$ samples (with $x = 0$, 0.3, 0.5, and 0.7) corresponds to that of the standard CuO as seen in Fig. 5(a). Therefore, it can be concluded that the oxidation state of copper in the samples is +2. At the Fe *K* edge, a comparison of edge energy of all the samples with

TABLE I. Structural parameters of the $Cu_{1-x}Ni_xFe_2O_4$ samples estimated from Rietveld refinement: lattice constant (*a*), unit cell volume (*V*), oxygen coordinate (*x*(O)), crystallite size (*D*), microstrain ($\Delta a/a$), and fitting quality (χ^2 and R_{wp}).

Sample	$CuFe_2O_4$	$Cu_{0.7}Ni_{0.3}Fe_2O_4$	$Cu_{0.5}Ni_{0.5}Fe_2O_4$	$Cu_{0.3}Ni_{0.7}Fe_2O_4$	$NiFe_2O_4$
a (Å)	8.377(1)	8.373(1)	8.370(1)	8.363(1)	8.344(2)
V (Å^3)	587.85(2)	586.91(1)	586.32(3)	584.91(3)	580.85(3)
x(O)	0.250(2)	0.251(1)	0.251(1)	0.252(2)	0.259(1)
D (nm)	22.1(1)	24.7(2)	29.4(1)	24.3(1)	5.6(1)
$\Delta a/a$	$5.8(2) \times 10^{-3}$	$12.6(1) \times 10^{-3}$	$14.4(1) \times 10^{-3}$	$7.5(3) \times 10^{-3}$	$4.6(2) \times 10^{-3}$
χ^2	1.36	1.19	1.25	1.31	1.37
R_{wp} (%)	11.0	5.07	6.45	7.22	9.04

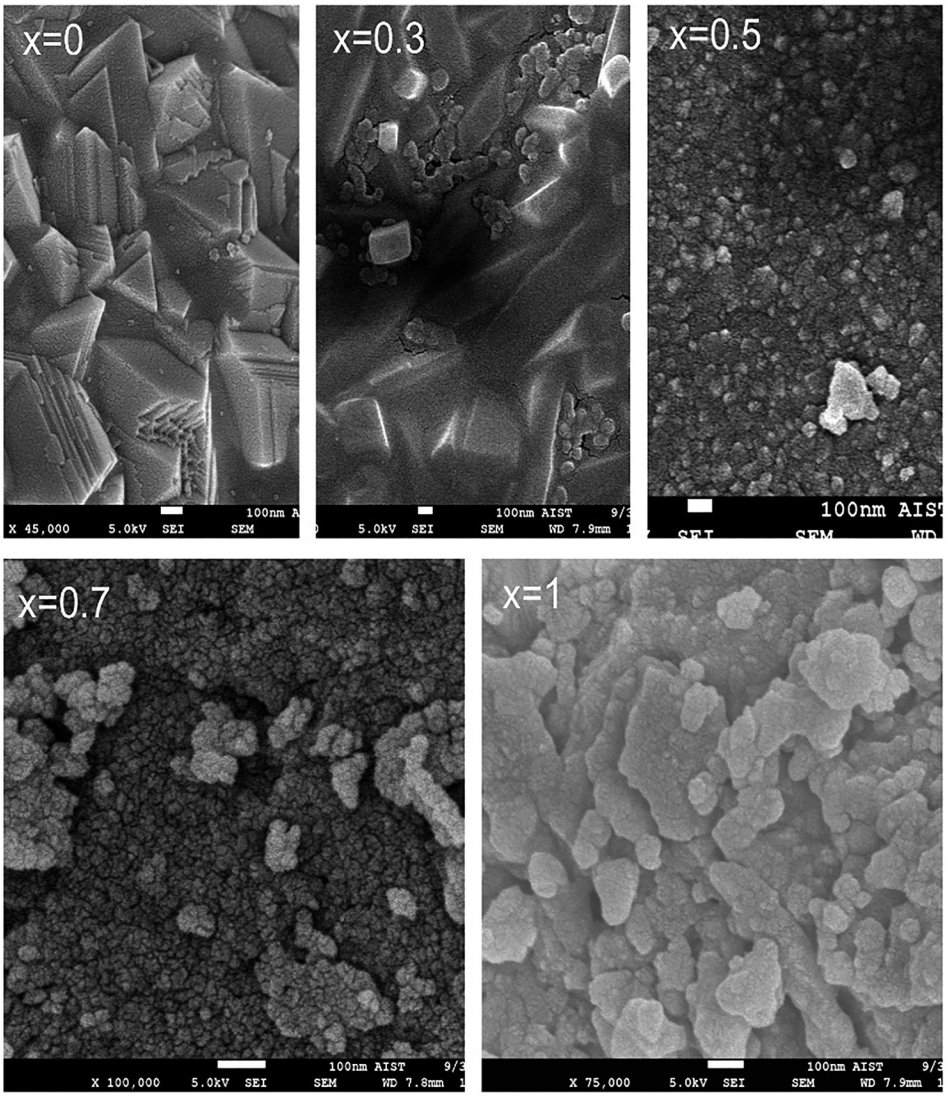

FIG. 4. Scanning electron microscopy images of the $Cu_{1-x}Ni_xFe_2O_4$ samples ($x = 0$, 0.3, 0.5, 0.7, and 1).

those of the iron oxide standards shows that the samples contain some Fe^{2+} in addition to Fe^{3+}. The fraction $\sum[Fe^{2+}]/\sum[Fe]$ was calculated and listed in Table II. The presence of Fe^{2+} in the samples can be explained due to partial reduction of Cu^{2+} to Cu^{+} at high temperature via the sequence of reactions: $2CuO \rightarrow Cu_2O + {}^1/_2O_2$, then $Cu_2O + Fe_2O_3 \rightarrow 2CuFeO_2$.[29] Hence, the samples with richer copper concentration have higher fraction $\sum[Fe^{2+}]/\sum[Fe]$ as seen in the table. The presence of Fe^{2+} ions may be due to oxygen deficiency in the samples.

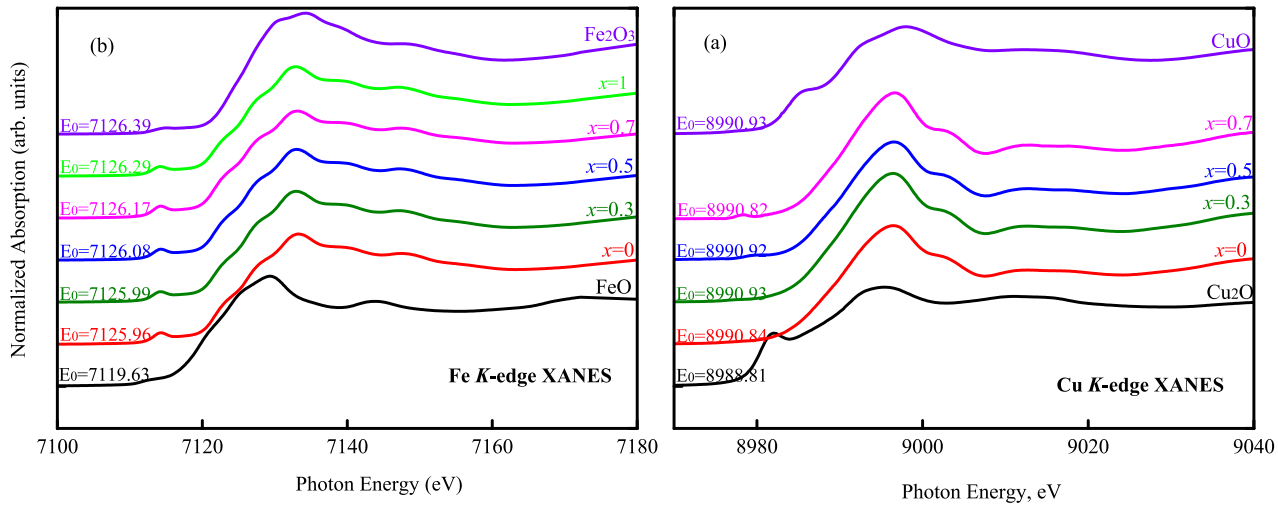

FIG. 5. Normalized Cu (a) and Fe (b) *K*-edges XANES spectra of the $Cu_{1-x}Ni_xFe_2O_4$ samples and the standards.

TABLE II. Concentration of Fe^{2+} in the $Cu_{1-x}Ni_xFe_2O_4$ samples.

x	0	0.3	0.5	0.7	1
$\sum[Fe^{2+}]/\sum[Fe]$ (%)	6.36	5.91	4.58	3.25	1.47

B. Magnetic characterization

The magnetization as a function of external magnetic field for all the samples was measured at different temperatures from 88 K to 900 K. For example, Fig. 6 shows the *M–H* curves of the samples measured at 88 K and 298 K. Within the investigated magnetic field range, most of the magnetization curves do not reach the saturation state, especially those measured at low temperatures. This may be explained due to random distribution of the magnetization directions of the nanoparticles in the samples. In order to estimate the saturation magnetization *M*s of the samples at each measuring temperature, we could apply the law of approach to saturation describing the magnetization as a function of magnetic field as follows:[30,31]

$$M = Ms(1 - a/H^{1/2} - b/H^2), \quad (1)$$

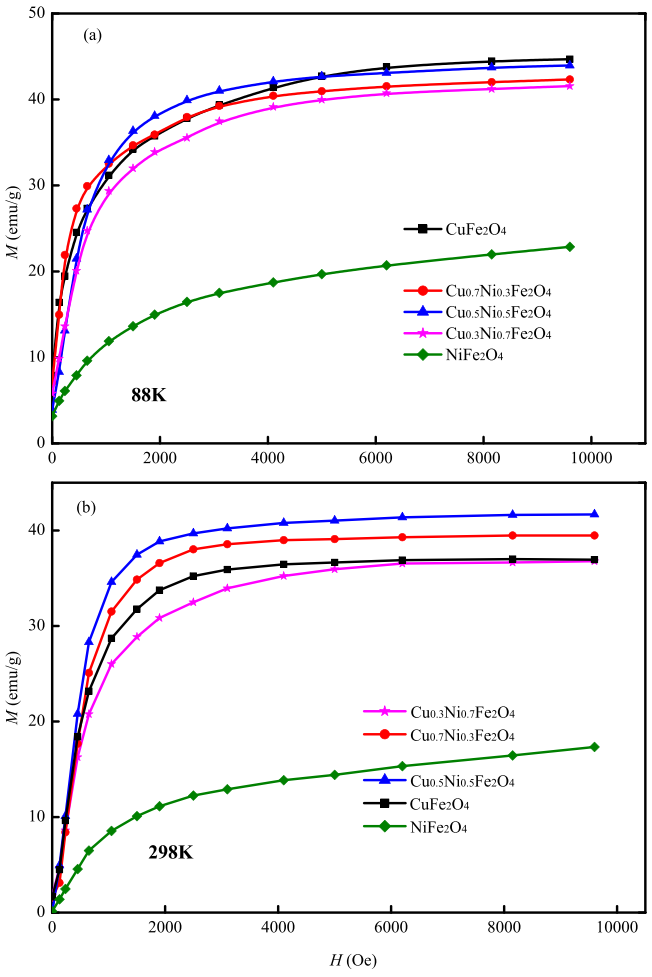

FIG. 6. *M–H* curves measured at 88 K and 298 K for the $Cu_{1-x}Ni_xFe_2O_4$ samples ($x = 0$, 0.3, 0.5, 0.7, and 1). Dots are the experimental values and solid lines are fits to the experimental data according to Eq. (1).

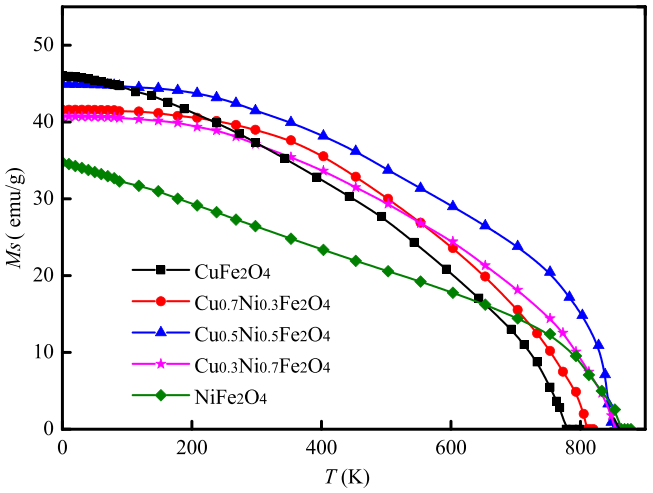

FIG. 7. Temperature dependence of saturation magnetization of the $Cu_{1-x}Ni_xFe_2O_4$ samples ($x = 0$, 0.3, 0.5, 0.7, and 1).

where the term $a/H^{1/2}$ arises from defects in the particles and the term b/H^2 is attributed to the effective anisotropy energy of the samples. The fitting curves to the experimental data points according Eq. (1) are also presented in Fig. 6. The temperature dependence of the fitted *M*s values using Eq. (1) is shown in Fig. 7.

The saturation magnetization at zero Kelvin *M*s(0) was extrapolated based on the *M*s data at temperature region below 300 K (Fig. 7) using the modified Bloch's function for spin wave $Ms(T) = Ms(0)[1 - BT^{\alpha}]$, where B is a constant and α is the Bloch exponent.[32] From the extrapolated saturation magnetization data, the corresponding magnetic moment values n_B^{exp} in the Bohr magneton per formula unit were determined for the samples using the relation:[33] $n_B^{exp} = \frac{Ms \times M_W}{5585}$, where M_W is the molecular weight of the sample and *M*s is the saturation magnetization in emu/g. The results are presented in Table III.

From Table III, it is seen that the saturation magnetization at 0 K of the $Cu_{1-x}Ni_xFe_2O_4$ samples has a decreasing tendency upon substitution of Ni for Cu. However, the *M*s values do not vary monotonously as *M*s of the sample with $x = 0.5$ is larger than that of the sample $x = 0.3$. It is expected that the magnetization is strongly affected by the concentration changes of magnetic ion species and their distribution in the lattice. The influence of cation distribution in saturation magnetization will be discussed in more details in Sec. C. The decrease in particle size also leads to a reduction in magnetization, especially for the samples with mean particle diameter below approximately 10-20 nm.[34] In this size range, the contribution of the disordered spins in the surface regions to the total magnetic moments of the particles becomes significant.

The Curie temperature of the samples was determined from the *M*s-*T* curves presented in Fig. 7 and taken as temperature at which *M*s vanishes. The values of the Curie temperature T_C for the samples are presented in Table III. The Curie temperature increases with increasing Ni content from 770 K for $CuFe_2O_4$ to 860 K for $NiFe_2O_4$. The T_C values of the $CuFe_2O_4$ and $NiFe_2O_4$ samples are in agreement with that reported earlier for the sample prepared by the solid reaction

TABLE III. Cation distribution, extrapolated magnetization at 0 K ($Ms(0)$), magnetic moment values n_B, and thickness of spin-disordered surface layer d of the $Cu_{1-x}Ni_xFe_2O_4$ samples.

				Magnetic moment (μ_B/f.u.)			
x	Cation distribution	$Ms(0)$ (emu/g)	T_C (K)	n_B^{theo}	$n_B^{theo'}$	n_B^{exp}	d (nm)
0	$(Cu_{0.15}\,Fe_{0.85})_A$ $[Cu_{0.15}\,Fe_{1.15}]_B$	46.0	770	2.2	2.07	1.98	…
0.3	$(Cu_{0.055}\,Fe_{0.945})_A$ $[Cu_{0.645}Ni_{0.3}Fe_{1.055}]_B$	41.6	808	1.8	1.70	1.77	…
0.5	$(Cu_{0.052}\,Fe_{0.948})_A$ $[Cu_{0.448}Ni_{0.5}Fe_{1.052}]_B$	45.0	841	2.02	1.92	1.92	…
0.7	$(Fe)_A[Cu_{0.3}Ni_{0.7}Fe]_B$	40.7	850	1.84	1.78	1.72	…
1	$(Fe)_A[NiFe]_B$	34.7	860	2.2	2.17	1.46	0.35

method.[35,36] It is known that the Curie temperature of spinel ferrites depends on the strength of intersublattice exchange interaction which is manifested by the exchange integral J_{AB}. Because $J_{Fe(A)\text{-}Ni[B]}$ in $NiFe_2O_4$ is larger than $J_{Cu(A)\text{-}Fe[B]}$ in $CuFe_2O_4$,[37] when Cu^{2+} is replaced by Ni^{2+}, the exchange integral J_{AB} is increased, and hence T_C also increases.

C. Cation distribution

Figure 8 shows the Fourier transforms (FTs) of EXAFS data for the $Cu_{1-x}Ni_xFe_2O_4$ samples at the Fe K edge to obtain the radial distribution functions. In this form, the data directly reflect the average local environment around the absorbing atoms where the peaks in the FTs typically represent shells of atoms around the absorber. The range of wave number k for Fourier transformation was $2 < k < 14$ Å^{-1}. The first peak in the FTs at about 1.1 Å corresponds to iron coordinated to oxygen in the (A) site, the second peak at about 1.5 Å corresponds to iron coordinated to oxygen in the [B] site, the third one at about 2.6 Å corresponds to the iron-metal distance between the neighboring octahedral sites, and the fourth peak at about 3.1 Å is due to the iron-metal distance between the neighboring octahedral and tetrahedral sites.[38] The difference in the FT profiles of the samples, especially the appearance of first FT peak, can be seen in Fig. 8. For the $Cu_{1-x}Ni_xFe_2O_4$ samples with $x = 0.7$ and 1, the FT profiles are similar to the one of the inverse spinel Fe_3O_4,[39,40] suggesting that these samples also have inverse spinel structure, whereas the FTs of the $Cu_{1-x}Ni_xFe_2O_4$ samples with $x = 0$, 0.3, and 5 are similar to those of the mixed spinel structures as reported for $CuFe_2O_4$.[41] In addition, it was also observed that the first FT peak of all the samples shifts to lower radial coordinate R when copper concentration increases. This is an indication that the divalent ions (Cu^{2+} or/and Ni^{2+}) occupy the tetrahedral sites in the samples with higher copper content. On the other hand, the saturation magnetization calculated from the VSM data also reveals the presence of divalent ions in the tetrahedral sites in the samples with $x = 0$, 0.3, and 0. 5. If we assume that Ni^{2+} and Cu^{2+} ions occupy only in the octahedral sites, then the magnetic moment values per formula unit are estimated to be 1.84 μ_B and 2.2 μ_B, respectively, for the samples with $x = 0.7$ and 1 according to the Néel model for two magnetic sublattices. These values are higher than the experimental values obtained from the VSM measurements (see Table III), and this phenomenon can be explained due to the surface effect, whereas for the $Cu_{1-x}Ni_xFe_2O_4$ samples with $x = 0$, 0.3, and 0.5, the magnetic moment values will be, respectively, 1 μ_B, 1.36 μ_B, and 1.6 μ_B, which are much lower than the measured values from VSM (given in Table III). This observation can be explained by the fact that in these samples, an amount of divalent ions migrates from the [B] to (A) sites under the quenching process that leads to the increase in the magnetic moment. The reported studies on Ni-Cu ferrites indicated that Cu^{2+} ions can occupy in both the tetrahedral and octahedral sites, but Ni^{2+} ions prefer to reside in the tetrahedral sites only.[15,16,42] If some percentages of copper atoms occupy the tetrahedral site, then an equal number of iron atoms will move to the octahedral site.[43] The cation distribution for $Cu_{1-x}Ni_xFe_2O_4$ compositions can then be written as $(Cu_yFe_{1-y})_A[Ni_xCu_{1-x-y}Fe_{1+y}]_B$. This model is in agreement with the model estimated from the Mössbauer study of the bulk copper-nickel ferrite.[44]

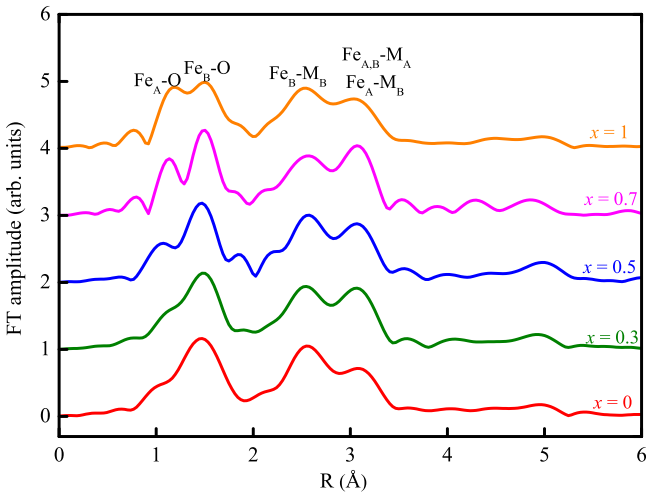

FIG. 8. Fourier transform profiles of the k-weighted EXAFS spectra of the $Cu_{1-x}Ni_xFe_2O_4$ samples at Fe K edge.

In the following, we apply the above model for cation distribution to Rietveld analysis of SXRD data. In this analysis, we have performed many versions of processing with changing of the site occupancy factors of Cu^{2+} and Fe^{3+} ions in the (A) and [B] sites. The refinement results for cation distribution in the samples are listed in Table III, which were obtained with the best fitting quality parameters χ^2 and

R_{wp} as given in Table I. The samples with nickel contents $x = 0.7$ and 1 have complete inverse spinel structure in which Ni^{2+} and Cu^{2+} ions occupy in the octahedral sites only. For the samples with $x = 0$, 0.3, and 0.5, Cu^{2+} ions distribute in both the (A) and [B] sites, and the concentration of Cu^{2+} ions in (A) site increases with increasing copper content. The theoretical magnetic moment ($n_B{}^{theo}$) per one formula unit was calculated for the samples using cation distribution results derived from Rietveld analysis by using the Néel model

$$n_B{}^{theo} = [2.2x + (1 - x - y) + 5(1 + y)] - [y + 5(1 - y)]. \quad (2)$$

In the calculation, the spin values of Fe^{3+} ($S = 5/2$, $g = 2$), Cu^{2+}($S = 1/2$, $g = 2$), and Ni^{2+}($S = 1$, $g = 2.2$) were used. The theoretical magnetic moment values denoted as $n_B{}^{theo}$ are presented in Table III. The magnetic moment values determined from magnetization measurements are found to be lower than those estimated via Rietveld refinement. However, Eq. (2) does not take into account the presence of Fe^{2+} ions in the samples. As derived from XANES analysis (Table II), all the samples contain a small amount of Fe^{2+} ion with lower spin number ($S = 2$), which could be a possible source for the reduction of magnetic moments. If we assume that Fe^{2+} ions occupy only in the octahedral sites like in the case of Fe_3O_4,[40] then the cation distribution of $Cu_{1-x}Ni_xFe_2O_4$ samples is written as $(Cu^{2+}{}_yFe^{3+}{}_{1-y})_A$ $[Ni^{2+}{}_xCu^{2+}{}_{1-x-y}Fe^{2+}{}_\delta Fe^{3+}{}_{1+y-\delta}]_B$, and the magnetic moment per one formula unit is calculated as follows:

$$n_B{}^{theo'} = [2.2x + (1 - x - y) + 5(1 + y - \delta) + 4\delta] - [y + 5(1 - y)], \quad (3)$$

where δ is the Fe^{2+} concentration in the samples taken from Table II. The calculated magnetic moment values according to Eq. (3) are denoted as $n_B{}^{theo'}$ and are also listed in Table III. For the samples with $x = 0$, 0.3, 0.5, and 0.7, the magnetic moment values $n_B{}^{theo'}$ are in good agreement with the magnetic moment values determined from magnetization measurements, whereas for the $NiFe_2O_4$ sample which has the smallest crystallite size, the $n_B{}^{theo'}$ value is higher than that determined from magnetization measurements (see Table III). This effect can be explained reasonably based on the spin disorder in surface shell regions. Assuming the core-shell model applying to spherical nanoparticles in which the core orders ferrimagnetically and the shell is magnetically disordered, the thickness of the surface shell d is calculated from the formula:[45] $n_B^{exp} = n_B^{theo'}\left(\frac{(D/2)-d}{D/2}\right)^3$, where D is the diameter of the nanoparticles. In the calculation, D values are taken as the average crystallite size given in Table I. The average shell thickness value d equals to 0.35 nm (see Table III) which is less than a unit cell length of the sample.

IV. CONCLUSIONS

Nanosized nickel-substituted copper ferrites ($Cu_{1-x}Ni_xFe_2O_4$ with $x = 0$, 0.3, 0.5, 0.7, and 1) were successfully synthesized by using the spray co-precipitation method and annealed at $T_a = 900\,°C$. All the samples were found to crystallize in cubic structure in which the lattice parameter and the average grain size decrease with increasing nickel content. The presence of Fe^{2+} ions was detected in all the samples showing that Fe^{2+} amount decreases with increasing nickel concentration. Cation distribution of all the samples was determined, indicating that Cu^{2+} ions distribute in both the tetrahedral and octahedral sites, while Ni^{2+} ions occupy only in the [B] site. It was shown that the distribution of Cu^{2+} ions in the (A) site (y) depends on Ni^{2+} content. The samples are mixed spinel in which y decreases when the nickel concentration increases from $x = 0$ to $x = 0.5$ and becomes complete inverse spinel when x reaches to 0.7. The decrease in y value and Fe^{2+} amount with increasing nickel content was confirmed to be the main reason affecting the saturation magnetization of the samples. For the sample with $x = 1$ which has the smallest grain size, the saturation magnetization was strongly affected by the surface contribution. With Ni^{2+} content increasing from 0 to 1, the Curie temperature T_C increases monotonously. Our work showed that spray co-precipitation is an efficient method to fabricate Cu–Ni ferrites in large scales, with tunable particle size and magnetic properties.

ACKNOWLEDGMENTS

This work was financially supported by the Vietnam National Foundation for Science and Technology Development under Grant No. 103.02-2015.32.

[1]A. Goldman, *Modern FerriteTechnology*, 2nd ed. (Springer, Pittsburgh, 2006), p. 438.
[2]S. C. McBain, H. HP. Yiu, and J. Dobson, Int. J. Nanomed. **3**, 169 (2008).
[3]R. Valenzuela, Phys. Res. Int. **2012**, 1 (2012).
[4]C. N. Chinnasamy, A. Narayanasamy, N. Ponpandian, K. Chattopadhyay, K. Shinoda, B. Jeyadevan, K. Tohji, K. Nakatsuka, T. Furubayashi, and I. Nakatani, Phys. Rev. B **63**, 184108 (2001).
[5]N. Marinoni, D. Levy, M. Dapiaggi, A. Pavese, and R. I. Smith, Phys. Chem. Miner. **38**, 11 (2010).
[6]Z. Sun, L. Liu, D. Z. Jia, and W. Pan, Sens. Actuators, B **125**, 144 (2007).
[7]M. Estrella, L. Barrio, G. Zhou, X. Wang, Q. Wang, W. Wen, J. C. Hanson, A. I. Frenkel, and J. A. Rodriguez, J. Phys. Chem. C **113**, 14411 (2009).
[8]Y. Fu, Q. Chen, M. He, Y. Wan, X. Sun, H. Xia, and X. Wang, Ind. Eng. Chem. Res. **51**, 11700 (2012).
[9]E. J. Choi, J. Korean Phys. Soc. **50**, 460 (2007).
[10]B. D. Cullity and C. D. Graham, *Introduction to Magnetic Materials*, 2nd ed. (Wiley-IEEE Press, New Jersey, 2009) p. 568.
[11]T. F. Marinca, I. Chicinaş, and O. Isnard, Ceram. Int. **38**, 1951 (2012).
[12]S. M. Hoque, S. S. Kader, D. P. Paul, D. K. Saha, H. N. Das, M. S. Rana, K. Chattopadhyay, and M. A. Hakim, IEEE Trans. Magn. **48**, 1839 (2012).
[13]J. Feng, L. Su, Y. Ma, C. Ren, Q. Guo, and X. Chen, Chem. Eng. J. **221**, 16 (2013).
[14]N. Kim Thanh, N. Phuc Duong, D. Quoc Hung, T. Thanh Loan, and T. Duc Hien, J. Nanosci. Nanotechnol. **16**, 7949 (2016).
[15]H. M. Zaki, Physica B **407**, 2025 (2012).
[16]L. Wang, Z. Li, Y. Liang, and K. Zhao, Adv. Powder Technol. **25**, 1510 (2014).
[17]X. Tan, G. Li, Y. Zhao, and C. Hu, Mater. Res. Bull. **44**, 2160 (2009).
[18]S. M. Hoque, A. Choudhury, and F. Islam, J. Magn. Magn. Mater. **251**, 292 (2002).
[19]L. N. Anh, T. T. Loan, N. P. Duong, S. Soontaranon, T. T. Viet Nga, and T. D. Hien, J. Alloys Compd. **647**, 419 (2015).
[20]J. Rodríguez-Carvajal, Phys. B Condens. Matter **192**, 55 (1993).

[21]D. Balzar, *Voigt-Function Model in Diffraction Line-Broadening Analysis, Defects and Microstructure Analysis by Diffraction*, International Union of Crystallography, Monograph on Crystallography (Oxford University Press, Oxford, UK, 1999), p. 94.
[22]L. B. McCusker, R. B. Von Dreele, D. E. Cox, D. Louër, and P. Scardi, J. Appl. Crystallogr. **32**, 36 (1999).
[23]W. Klysubun, P. Sombunchoo, W. Deenan, and C. Kongmark, J. Synchrotron Radiat. **19**, 930 (2012).
[24]B. Ravel and M. Newville, J. Synchrotron Radiat. **12**, 537 (2005).
[25]L. Machala, J. Tuček, and R. Zbořil, Chem. Mater. **23**, 3255 (2011).
[26]A. M. Balagurov, I. A. Bobrikov, M. S. Maschenko, D. Sangaa, and V. G. Simkin, Crystallogr. Rep. **58**, 710 (2013).
[27]R. D. Shannon, Acta Crystallogr., Sect. A **32**, 751 (1976).
[28]A. Ahmed, P. Elvati, and A. Violi, RSC Adv. **5**, 35033 (2015).
[29]J. P. Doumerc, A. Wichainchai, A. Ammar, M. Pouchard, and P. Hagenmuller, Mater. Res. Bull. **21**, 745 (1986).
[30]H. Kronmuller, IEEE Trans. Magn. **15**, 1218 (1979).
[31]Z. Q. Jin, W. Tang, J. R. Zhang, H. X. Qin, and Y. W. Du, Eur. Phys. J. B **3**, 41 (1998).
[32]P. V. Hendriksen, S. Linderoth, and P.-A. Lindgård, J. Magn. Magn. Mater. **104–107**, 1577 (1992).
[33]M. A. Gabal, Y. M. Al Angari, and S. S. Al-Juaid, J. Alloys Compd. **492**, 411 (2010).
[34]N. T. Lan, N. P. Duong, and T. D. Hien, J. Alloys Compd. **509**, 5919 (2011).
[35]K. Roumaih, J. Alloys Compd. **465**, 291 (2008).
[36]G. F. Goya, H. R. Rechenberg, and J. Z. Jiang, J. Appl. Phys. **84**, 1101 (1998).
[37]S. Krupika and P. Novak, *Ferromagnetic Materials* (North-Holland, Amsterdam, 1982), p. 189.
[38]C. M. B. Henderson, J. M. Charnock, and D. A. Plant, J. Phys.: Condens. Matter **19**, 076214 (2007).
[39]Z. Beji, M. Sun, L. S. Smiri, F. Herbst, C. Mangeney, and S. Ammar, RSC Adv. **5**, 65010 (2015).
[40]G. Subías, J. García, and J. Blasco, Phys. Rev. B **71**, 155103 (2005).
[41]V. Krishnan, R. K. Selvan, C. O. Augustin, A. Gedanken, and H. Bertagnolli, J. Phys. Chem. C **111**, 16724 (2007).
[42]K. Roumaih, J. Mol. Struct. **1037**, 431 (2013).
[43]F. Kenfack and H. Langbein, J. Mater. Sci. **41**, 3683 (2006).
[44]P. Muthukumarasamy, T. Nagarajan, and A. Narayanasamy, J. Phys. C: Solid State Phys. **15**, 2519 (1982).
[45]A. Millan, A. Urtizberea, N. J. O. Silva, F. Palacio, V. S. Amaral, E. Snoeck, and V. Serin, J. Magn. Magn. Mater. **312**, 5 (2007).